

Topological phase transition under pressure in the topological nodal-line superconductor PbTaSe₂C. Q. Xu,^{1,2} R. Sankar,^{3,4} W. Zhou,¹ Bin Li,^{5,*} Z. D. Han,¹ B. Qian,^{1,*} J. H. Dai,² Hengbo Cui,⁶
A. F. Bangura,⁷ F. C. Chou,⁴ and Xiaofeng Xu^{1,2,*}¹*Advanced Functional Materials Lab and Department of Physics, Changshu Institute of Technology, Changshu 215500, China*²*Department of Physics, Hangzhou Normal University, Hangzhou 310036, China*³*Institute of Physics, Academia Sinica, Nankang, Taipei 11529, Taiwan*⁴*Center for Condensed Matter Sciences, National Taiwan University, Taipei 10617, Taiwan*⁵*Information Physics Research Center, Nanjing University of Posts and Telecommunications, Nanjing 210023, China*⁶*Condensed Molecular Materials Laboratory, RIKEN, Wako-shi, Saitama 351-0198, Japan*⁷*Max-Planck-Institut für Festkörperforschung, Heisenbergstr. 1, D-70569 Stuttgart, Germany*

(Received 8 June 2017; published 31 August 2017)

A first-order-like resistivity hysteresis is induced by a subtle structural transition under hydrostatic pressure in the topological nodal-line superconductor PbTaSe₂. This structure transition is quickly suppressed to zero at pressure ~ 0.25 GPa. As a result, superconductivity shows a marked suppression, accompanied with pronounced changes in the magnetoresistance and Hall resistivity. The first-principles calculations show that the spin-orbit interactions partially gap out the Dirac nodal line around K point in the bulk Brillouin zone upon applying a small pressure, whereas the Dirac states around H point are completely destroyed. The calculations further reveal a second structural phase transition under a pressure as high as ~ 30 GPa, through which a transition from a topologically nontrivial bulk phase to a trivial phase is uncovered, with a superconducting dome emerging under this high-pressure phase. Our calculations also reveal how the bulk Fermi surfaces and the surface bands evolve with pressure. This theoretical study shall inspire in-depth experimental investigations on the electronic structure of this novel topological superconductor under higher pressures.

DOI: [10.1103/PhysRevB.96.064528](https://doi.org/10.1103/PhysRevB.96.064528)**I. INTRODUCTION**

The recent development in topological physics has significantly extended the interest from an isolated Dirac node, either in two-dimensional (2D) surface states or in 3D semimetals, to the lines or loops of Dirac nodes that are protected by the interplay of symmetry and topology [1–4]. The Dirac nodal-line (DNL) semimetals have extended band touching of conduction and valence bands along a one-dimensional line in the momentum space and are expected to host a variety of exotic transport phenomena. Particular interest arises if these DNL semimetals also host superconductivity, which are often regarded as strong candidates of topological superconductors (TSCs) whose low-lying excitations may be described by Majorana fermions, defined as fermions that are their own antiparticles that are proposed to exist at the edge of a TSC [5]. However, the material realization of the TSCs is especially rare, in particular for ones with stoichiometric compositions. For example, although the topologically protected surface states have recently been claimed in the centrosymmetric superconductor β -PdBi₂ by angular-resolved photoemission spectroscopy (ARPES), unambiguous evidence in favor of such topological states from other experimental techniques is still lacking [6–9].

Among these TSC candidates, PbTaSe₂ is special, if not unique, in that its DNL states have been firmly identified by ARPES [10] and found to be rather robust against spin-orbit coupling (SOC), which often opens up a gap and induces topologically nontrivial band-inverted states [11,12].

In addition, its superconducting state exhibits many interesting properties, including the strong upward curvature in its H_{c2} and a V-shaped pressure dependence of T_c in the polycrystalline samples [13]. Further, its superconducting gap has been reported to be nodeless [14–16], meeting the requirement of a topological superconductor. Recent pressure measurements on single crystals, however, reveal a pronounced resistivity hysteresis associated with a subtle structure modification and a drastic suppression of T_c once $P \geq 0.25$ GPa [17]. The questions remain on how the DNL features are modified by this structural transition and to what extent the topological states can survive when subjected to higher pressures.

In this work, we report experimental transport measurements up to 2 GPa on high-purity single crystals of PbTaSe₂, combined with the first-principles calculations on its electronic structure up to 60 GPa, with a special emphasis on its topological features. Our experiments reveal a marked resistivity hysteresis upon the application of a small pressure. The superconducting T_c is quickly suppressed above ~ 0.25 GPa, accompanied by an abrupt change in other transport coefficients, such as residual resistivity, magnetoresistance (MR), and Hall resistivity. The calculations suggest this low- P phase transition at ~ 0.25 GPa is associated with a subtle change in its structure that opens up a small energy gap in a part of the DNL structure in the presence of SOC. Our calculations further uncover a phase transition from topological nontrivial bands to topological trivial states, induced by a second structure transition under ~ 30 GPa. Under this high- P phase, a superconducting dome is resolved on the assumption of electron-phonon mediated pairing. Our calculations also reveal the evolution of the bulk Fermi surfaces and the surface states

*xiaofeng.xu@cslg.edu.cn, libin@njupt.edu.cn, njqb@cslg.edu.cn

under pressure, which shall stimulate future high-pressure measurements in due course.

II. EXPERIMENT

High-quality single crystals of PbTaSe_2 were grown by chemical vapor transport method. The detailed process of synthesis was described in Ref. [18]. Magnetoresistance and the Hall effect measurements were performed by a standard four-probe lock-in technique in a Quantum Design PPMS at fields up to 9 Tesla in both positive and negative field polarities. Signal even (odd) in field was defined as magnetoresistance (Hall effect). For the hydrostatic pressure measurements, samples were loaded into a piston-type pressure cell and the actual pressure was determined by measuring the superconducting transition temperatures of Pb. Daphne 7373 oil was applied as the pressure transmission media. For the data under different pressures, the same contacts were used throughout the measurements such that the geometric errors in the contact size were identical for different runs.

To determine high-pressure structures, we used the evolutionary crystal structure prediction method USPEX [19–21]. Predictions were made from ambient pressure up to 60 GPa with a step of 5 GPa. Structure relaxations, enthalpy, and electron-phonon calculations were performed using the QUANTUM-ESPRESSO [22] code with ultrasoft pseudopotential method and the plane-wave basis. The cutoffs were chosen as 30 Ry for the wave functions and 300 Ry for the charge density. The generalized-gradient approximation of Perdew-Burke-Ernzerhof (PBE) [23] was used for the exchange-correlation energy function. The electronic structure calculations with high accuracy for the stable structures were performed using the full-potential linearized augmented plane-wave (FP-LAPW) method implemented in the WIEN2K code. [24] The generalized gradient approximation (GGA) [23] was applied to the exchange-correlation potential calculation. The muffin tin radii were chosen to be 2.5 a.u. for Pb and Ta, and 2.37 a.u. for Se. The plane-wave cutoff was defined by $RK_{\text{max}} = 7.0$, where R is the minimum LAPW sphere radius and K_{max} is the plane-wave vector cutoff. Spin-orbit coupling was included in the calculations. To obtain the Fermi surface and surface state properties, a tight-binding model based on maximally localized Wannier functions [25] was constructed to reproduce the bulk band structure including spin-orbit coupling with Pb s and p , Ta s and d , and Se p orbitals. Then Fermi surfaces and surface state spectrum of (001) surface for each phase were calculated with the surface Green's function methods as implemented in WANNIERTOOLS [26].

III. RESULTS

Figure 1(a) illustrates $\rho(T)$ profiles under various hydrostatic pressures (P). At ambient pressure, the T dependence of resistivity is typical of those reported in the literature [14–16]. Upon the application of a tiny pressure, e.g., 0.05 GPa, a sudden drop occurs around 286.5 K on the $\rho(T)$ curve during the cooling process. When warming up, the corresponding resistivity anomaly slightly shifts to a higher temperature, resulting in a pronounced hysteresis. Similar resistivity

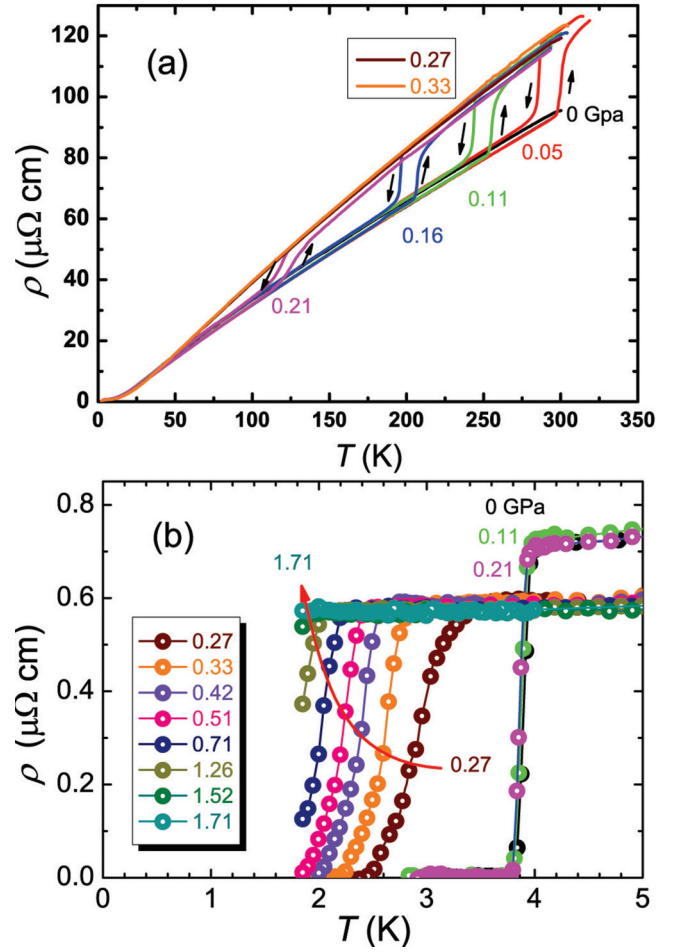


FIG. 1. (a) Temperature dependence of resistivity under different pressures. (b) An enlarged view of the resistivity curves at low temperatures.

hysteresis has recently been reported by Kaluarachchi *et al.*, which was ascribed to a subtle structural modification from the high- T $P\bar{6}m2(1e)$ phase to the low- T $P\bar{6}m2$ phase (see Fig. 5 for the corresponding structures). At ambient pressure, for example, with increasing T , the room temperature $P\bar{6}m2$ phase changes to $P\bar{6}m2(1e)$, which can be obtained by shifting the Pb atom from the 1a-Wyckoff coordinate in $P\bar{6}m2$ to the 1e-Wyckoff position without changing its overall symmetry. According to Kaluarachchi *et al.*, this structure transition takes place at 425 K under ambient pressure, i.e., a temperature higher than our measurements [17]. Compared with $P\bar{6}m2$, the high- T $P\bar{6}m2(1e)$ phase displays an obvious contraction in the c -axis length while the a axis is slightly expanded [17]. Here, we define the structural transition temperature T_s as the average of the characteristic temperatures of the resistivity anomalies on the cooling and heating processes. With increasing pressure, T_s is found to be fast suppressed and disappears at $P_c \sim 0.25$ GPa. Note that the data shown in Fig. 1 were taken in the pressure increasing process, however, the hysteresis was found to be reversible in the pressure decreasing process (data not shown for clarity).

In Fig. 1(b), a blowup of resistivity in the low- T regime clearly splits into two branches. At the low-pressure region

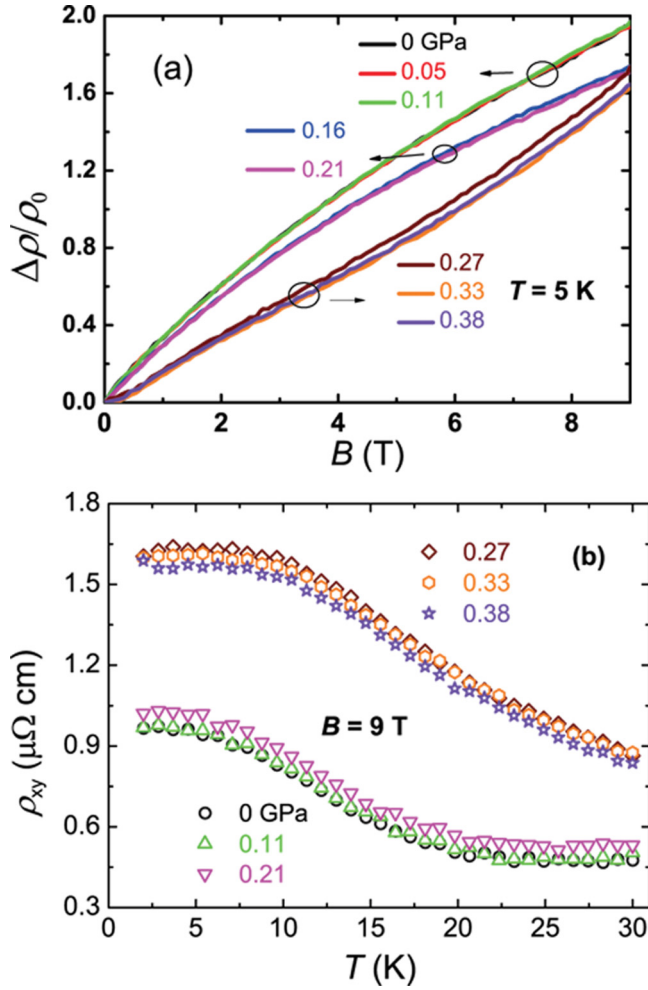


FIG. 2. (a) Magnetic field dependence of the magnetoresistance ($\Delta\rho/\rho_0$, $T = 5$ K) under different pressures. In our measurements, we changed the polarity of the field and the even signal in field was defined as MR. The odd signal in field was determined as Hall resistivity ρ_{xy} as shown in (b).

with $P \leq 0.21$ GPa, the sample shows sharp superconductivity with T_c around 3.9 K and T_c varies little with pressure. A notable suppression of T_c is clearly seen when P increases above 0.27 GPa. This suggests two superconducting phases are separated around $P_c \sim 0.25$ GPa. It is worth noting, this critical pressure is the same as the pressure where the resistivity hysteresis disappears, implying that these two superconducting phases correspond to different crystal structures. Besides, the residual resistivity, defined as the resistivity at 5 K, also shows a sudden drop across this critical pressure.

To gain further insight into the underlying electronic changes across this critical pressure, the magnetoresistance and the Hall resistivity are studied, as shown in Figs. 2(a) and 2(b), respectively. At low pressures, the field-dependent MR shows an interesting downward curvature, analogous to many recently discovered topological semimetals [27,28]. With increasing P , however, the size of MR is slightly reduced and the shape of MR becomes superlinear in field. Similar drastic changes across the critical pressure are also observable in the T -dependent Hall resistivity (ρ_{xy}) curves. When $P \geq P_c$, the

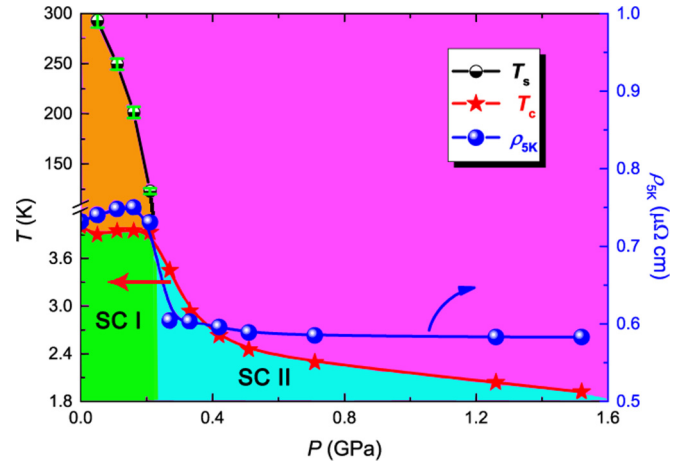


FIG. 3. Phase diagram for the pressure dependence of the structural transition temperature T_s , the superconducting transition temperature T_c , and the resistivity at 5 K (ρ_{5K}).

Hall resistivity is abruptly elevated, suggesting a pronounced change in the underlying electronic properties induced by the structural transition [29,30].

Based on the above transport data, the pressure-dependent phase diagram is summarized in Fig. 3. In this phase diagram, two distinct superconducting phases separated by a structural transition are resolved. The quick residual resistivity drop, along with the abrupt changes in the magnetoresistance and the Hall effects, clearly indicates the remarkable change in the electronic properties across the phase boundary.

To clarify the nature of transition between these two superconducting phases, detailed enthalpy calculations for different crystal structures are performed. The resultant enthalpy-pressure (ΔH - P) curves are plotted in Fig. 4, where the relative enthalpy differences ΔH are calculated with respect to the $P\bar{6}m2$ structure. We find that with increasing

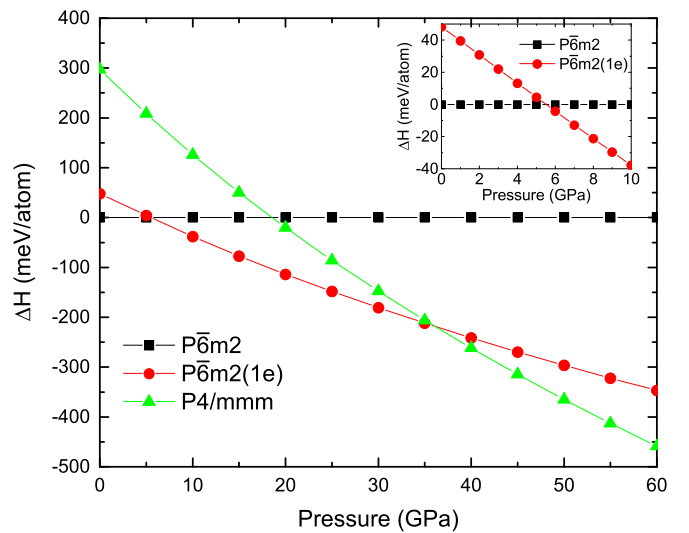


FIG. 4. Calculated enthalpies per atom as a function of pressure from 0–60 GPa with respect to $P\bar{6}m2$ structure. Inset shows the enlarged enthalpy comparison between $P\bar{6}m2$ and $P\bar{6}m2(1e)$ from 0–10 GPa.

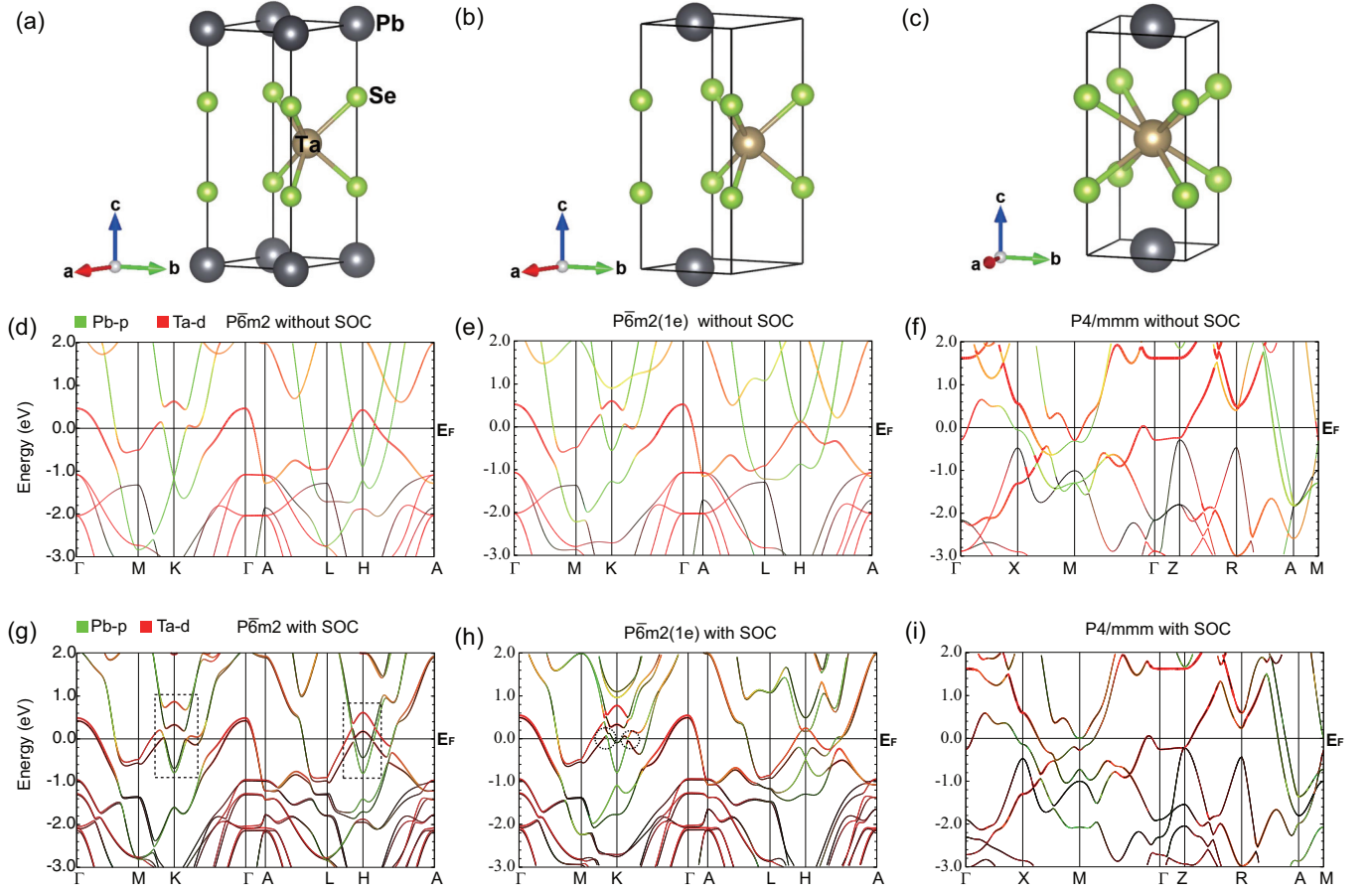


FIG. 5. The schematic unit cell for (a) noncentrosymmetric hexagonal $P\bar{6}m2$, (b) $P\bar{6}m2(1e)$, and (c) tetragonal $P4/mmm$ phases. The band structures of $PbTaSe_2$ calculated (d)–(f) without and (g)–(i) with SOC for three different structures. The weights of the Pb p and Ta d orbital contribution are color-coded by green and red, respectively. The rectangles in (g) indicate the DNL structure near K and H points. In (h), the DNL structure is gapped by SOC on the left-hand side of K but still intact on the right-hand side, indicated by the circles.

pressure, $PbTaSe_2$ undergoes two structural phase transitions, from the $P\bar{6}m2$ to $P\bar{6}m2(1e)$ structure at ~ 5 GPa, then to the tetragonal $P4/mmm$ structure at ~ 30 GPa. Below 5 GPa, the most stable structure is the $P\bar{6}m2$, which is the original phase found in experiment. As the pressure increases above ~ 5 GPa, the $P\bar{6}m2(1e)$ structure becomes more stable. Note that the $P\bar{6}m2(1e)$ structure shares the same global symmetry with $P\bar{6}m2$, with only the Pb atom shifting from the $1a$ Wyckoff position (0, 0, 0) to the $1e$ Wyckoff position ($2/3, 1/3, 0$) (see Fig. 5). At ambient conditions, the formation energy of the $P\bar{6}m2(1e)$ structure is 48.2 meV (~ 500 K) per atom higher than of the $P\bar{6}m2$ ground-state structure, the same energy scale as the structural transition around ~ 425 K observed in the high- T XRD and TEM experiments [17]. Our calculations suggest that the resistivity hysteresis observed at low pressures is indeed associated with this subtle structural transition, in line with those reported by Kaluarachchi *et al.* [17]. We also note that the critical pressure from the calculations (~ 5 GPa) is overestimated by a factor of 20 compared with the experimentally observed value (~ 0.25 GPa). This overestimation is an inherent issue in DFT calculations. At higher pressures, our study further predicted a new structural transition from $P\bar{6}m2(1e)$ to the tetragonal

structure with space group $P4/mmm$ above 30 GPa, revealing a second structural phase transition under pressure.

It is intriguing to see how the electronic structure changes with these structural transitions. The calculated bulk band structures without and with SOC for different structures are shown in Fig. 5. Our results for the noncentrosymmetric hexagonal $P\bar{6}m2$ [Figs. 5(d), 5(g)] are in good agreement with the previous reports [10–12, 18]. Large SOC splitting is clearly visible at the K and H points in the Brillouin zone for both Pb and Ta orbitals. The electronlike Pb p orbital and holelike Ta d orbital cross each other at the Fermi level, resulting in the nodal-line states at the K and H points, topologically protected by mirror reflection symmetry. Figures 5(e), 5(h) represent the band structure of $P\bar{6}m2(1e)$ phase. The band structure is overall similar to that in the $P\bar{6}m2$ except that the nodal-line states around the H point are completely destroyed. In this phase, nodal-line states at K point are partially gapped out by SOC. Figures 5(f), 5(i) delineate the band structure of $P4/mmm$ phase, which is completely distinct from the above two phases. A band crossing exists at M point but with no band inversion [see Fig. 5(f)] and a gap is induced by SOC [see Fig. 5(i)], which suggests a topologically trivial phase in this high-pressure structure.

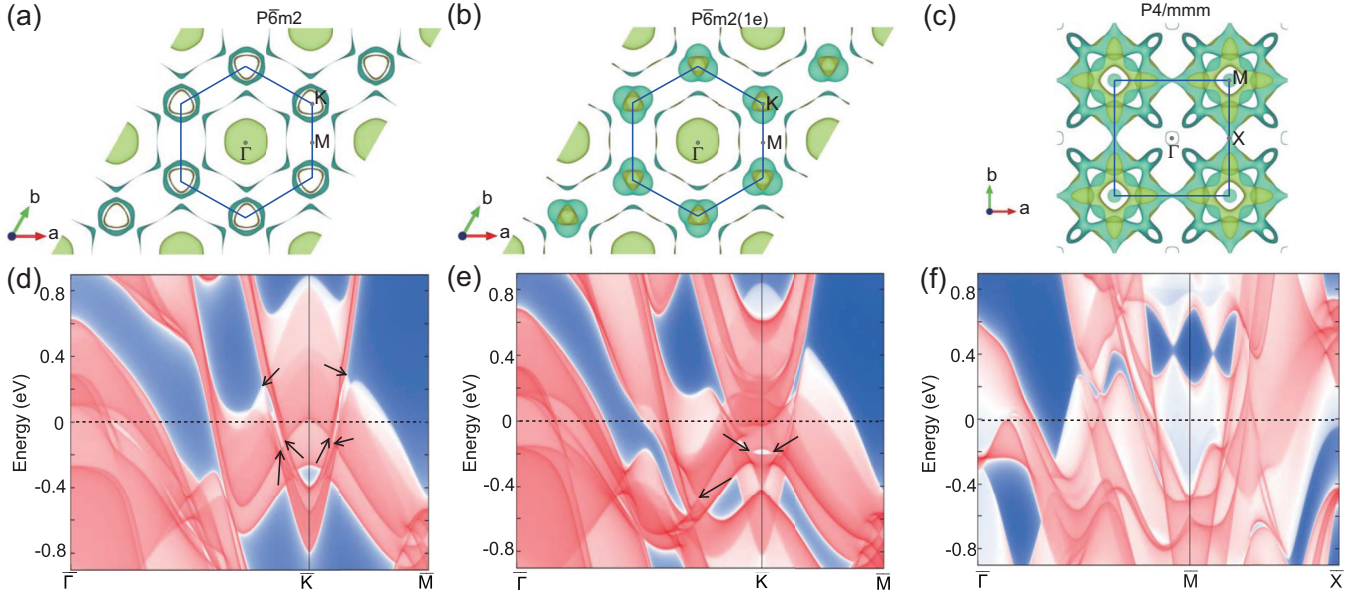


FIG. 6. Top: Calculated Fermi surfaces (FSs) of (a) $P\bar{6}m2$, (b) $P\bar{6}m2(1e)$, and (c) $P4/mmm$ phases. The blue boundary lines denote the first Brillouin zones (BZs). In $P\bar{6}m2$ and $P\bar{6}m2(1e)$ phases, there are two bands crossing the Fermi level, which construct the Fermi surfaces, while three bands cross the Fermi level in the high-pressure $P4/mmm$ phase. It is clear to see the Fermi surface nesting at the corners in the hexagonal phases, and the shape of these FSs changes from a cylinder to a dumbbell accompanied with the phase transition from $P\bar{6}m2$ to $P\bar{6}m2(1e)$. The FS pockets at the corner become more three dimensional from $P\bar{6}m2$ to $P\bar{6}m2(1e)$. Bottom: Surface state spectrum of (001) surfaces along $\bar{\Gamma}-\bar{K}-\bar{M}$ for (d) $P\bar{6}m2$, (e) $P\bar{6}m2(1e)$ phases, and bands along $\bar{\Gamma}-\bar{M}-\bar{X}$ for (f) $P4/mmm$ phase. The black arrows indicate the positions of Dirac nodes along the k path of the first BZ.

The resultant bulk Fermi surfaces from scalar-relativistic calculations are shown in Figs. 6(a)–6(c) for $P\bar{6}m2$, $P\bar{6}m2(1e)$, and $P4/mmm$ phases, respectively. For the hexagonal phases $P\bar{6}m2$ and $P\bar{6}m2(1e)$, there are two bands crossing the Fermi level. For $P\bar{6}m2$, the Fermi surfaces consist of three parts: a disk-shaped hole pocket centered at Γ , a hexagon-shaped electron pocket surrounding the disk-shaped pocket, and two nesting polygon cylinders at each corner of K points. The band analysis demonstrates that, distinct from the pockets surrounding Γ , the cylinders at the corner are hybridized from electron and hole bands, and Pb-derived bands dominate the electron part (inner pocket) while Ta-derived bands dominate the holelike part (outer pocket). For $P\bar{6}m2(1e)$, the disk-shaped and hexagon-shaped pockets are nearly intact, while the cylinders at corner shrink and become more three dimensional, and reconstruct to two dumbbell-shaped pockets. For high-pressure tetragonal $P4/mmm$ phase, three bands crossing the Fermi level construct a series of complicated three-dimensional Fermi surfaces: a cylinder centering at Γ , and a clover-shaped pocket overlapping with a petal-shaped pocket surrounding M point at the corner.

We further calculate the surface band structures using a tight-binding model based on maximally localized Wannier functions [25,26] constructed with Pb s and p , Ta s and d , and Se p orbitals. The surface bands are shown in Fig. 6(d)–6(f) for each phase. In $P\bar{6}m2$ phase, due to the reflection symmetry, gap opening is forbidden at the crossing points, which results in a nodal ring structure. In $P\bar{6}m2(1e)$ phase, Pb atom shifts from the $1a$ -Wyckoff position $(0, 0, 0)$ to the $1e$ -Wyckoff position $(2/3, 1/3, 0)$ without changing its reflection symmetry. As a

result, the band structure and surface states around \bar{K} point are similar to those of the $P\bar{6}m2$ phase. In contrast, for the

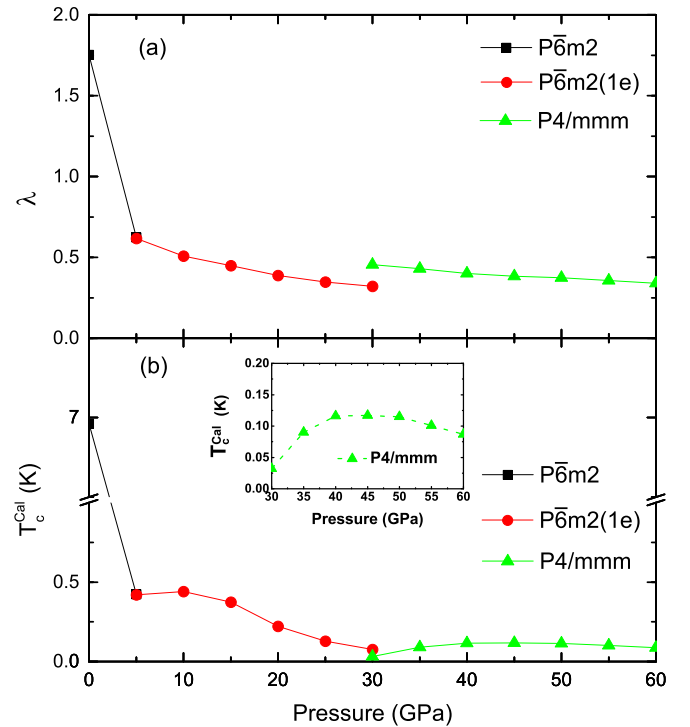


FIG. 7. (a) Electron-phonon coupling constant λ , and (b) superconducting T_c^{Cal} as a function of pressure. Inset shows the blowup of the superconducting dome in $P4/mmm$ phase.

tetragonal $P4/mmm$ phase, the surface band structure seems featureless, as plotted in Fig. 6(f).

In order to estimate the superconducting characteristics of PbTaSe_2 under pressure, we performed linear response calculations [31] of its electron-phonon properties, and estimated the critical temperature through the Mc-Millan Allen-Dynes formula [32,33]

$$T_c^{\text{Cal}} = \frac{\omega_{\text{ln}}}{1.2} \exp \left[-\frac{1.04(1 + \lambda)}{\lambda - \mu^*(1 + 0.62\lambda)} \right], \quad (1)$$

where ω_{ln} is the logarithmically averaged phonon frequency, and μ^* is the Coulomb pseudopotential, which is set to be 0.1 in the calculations. We evaluate the pressure-dependent electron-phonon coupling constants λ and the superconducting transition temperature T_c^{Cal} shown in Fig. 7. It is found that both λ and T_c^{Cal} are maximal in $P\bar{6}m2$ phase at 0 GPa. Note that T_c^{Cal} is twice the actual value of T_c observed in the experiments. As the pressure increases, both λ and T_c^{Cal} decrease up to 30 GPa. For the $P4/mmm$ phase, while the electron-phonon coupling constant slightly decreases with pressure, T_c^{Cal} demonstrates a superconducting dome, reaching a maximum value of 0.12 K at ~ 45 GPa. However, this small value of T_c makes the experimental verification very difficult.

IV. CONCLUSIONS

In conclusion, we have studied the high-pressure superconducting phase diagram of PbTaSe_2 from both experiments and first-principles calculations. Superconductivity shows a marked suppression above ~ 0.25 GPa, along with drastic changes in the magnetoresistance and Hall resistivity. The

first-principles calculations unveil the structural origin for this change, due to the shifting of the Pb atom from one Wyckoff coordinate to the other without changing its global symmetry. As a result, the nodal-line structure at the K point is partially gapped while the Dirac states around the H point are totally stripped away. The calculations further reveal a second structural transition at ~ 30 GPa, which is accompanied with a topological phase transition, from a topologically nontrivial state to a topologically trivial state. In this new state, a superconducting dome of electron-phonon interaction in its pairing origin is uncovered in the calculations. The Fermi surface and surface band structure are also investigated. In a word, our calculations reveal how the electronic states of PbTaSe_2 , especially its Dirac nodal states, both in the bulk and on the surface, evolve with pressure, which certainly motivates the need for more experimental investigations in due course.

ACKNOWLEDGMENTS

The authors would like to thank Nigel Hussey, and C. M. J. Andrew for the fruitful discussion. This work is sponsored by the National Key Basic Research Program of China (Grant No. 2014CB648400), and by National Natural Science Foundation of China (Grants No. 11474080, No. U1732162, No. 11504182, and No. 11374043), the Natural Science Foundation of Jiangsu Province (Grant No. BK20150831), Natural Science Foundation of Jiangsu Educational Department (Grant No. 15KJA430001), and six-talent peak of Jiangsu Province (Grant No. 2012-XCL-036). X.X. would also like to acknowledge the financial support from an open program from Wuhan National High Magnetic Field Center (Grant No. 2015KF15).

C.Q.X., R.S., and W.Z. contributed equally to this work.

-
- [1] R. Yu, H. M. Weng, Z. Fang, X. Dai, and X. Hu, Topological Node-Line Semimetal and Dirac Semimetal State in Antiperovskite Cu_3PdN , *Phys. Rev. Lett.* **115**, 036807 (2015).
 - [2] Y. Kim, B. J. Wieder, C. L. Kane, and A. M. Rappe, Dirac Line Nodes in Inversion-Symmetric Crystals, *Phys. Rev. Lett.* **115**, 036806 (2015).
 - [3] K. Mullen, B. Uchoa, and D. T. Glatzhofer, Line of Dirac Nodes in Hyperhoneycomb Lattices, *Phys. Rev. Lett.* **115**, 026403 (2015).
 - [4] Y. Wu *et al.*, Dirac node arcs in PtSn_4 , *Nat. Phys.* **12**, 667 (2016).
 - [5] M. Z. Hasan and C. L. Kane, Topological insulators, *Rev. Mod. Phys.* **82**, 3045 (2010).
 - [6] M. Sakano, K. Okawa, M. Kanou, H. Sanjo, T. Okuda, T. Sasagawa, and K. Ishizaka, Topologically protected surface states in a centrosymmetric superconductor $\beta\text{-PdBi}_2$, *Nat. Comm.* **6**, 8595 (2015).
 - [7] E. Herrera *et al.*, Magnetic field dependence of the density of states in the multiband superconductor $\beta\text{-Bi}_2\text{Pd}$, *Phys. Rev. B* **92**, 054507 (2015).
 - [8] J. Kačmarčík *et al.*, Single-gap superconductivity in $\beta\text{-Bi}_2\text{Pd}$, *Phys. Rev. B* **93**, 144502 (2016).
 - [9] L. Q. Che, T. Le, C. Q. Xu, X. Z. Xing, Z. X. Shi, Xiaofeng Xu, and Xin Lu, Absence of Andreev bound states in $\beta\text{-PdBi}_2$ probed by point-contact Andreev reflection spectroscopy, *Phys. Rev. B* **94**, 024519 (2016).
 - [10] G. Bian *et al.*, Topological nodal-line fermions in spin-orbit metal PbTaSe_2 , *Nat. Commun.* **7**, 10556 (2016).
 - [11] M. N. Ali, Q. D. Gibson, T. Klimczuk, and R. J. Cava, Non-centrosymmetric superconductor with a bulk three-dimensional Dirac cone gapped by strong spin-orbit coupling, *Phys. Rev. B* **89**, 020505(R) (2014).
 - [12] S.-Y. Guan *et al.*, Superconducting topological surface states in the noncentrosymmetric bulk superconductor PbTaSe_2 , *Sci. Adv.* **2**, e1600894 (2016).
 - [13] J. Wang *et al.*, Upward curvature of the upper critical field and the V-shaped pressure dependence of T_c in the noncentrosymmetric superconductor PbTaSe_2 , *J. Supercond. Nov. Magn.* **28**, 3173 (2015).
 - [14] C.-L. Zhang, Z. Yuan, G. Bian, S.-Y. Xu, X. Zhang, M. Z. Hasan, and S. Jia, Superconducting properties in single crystals of the topological nodal semimetal PbTaSe_2 , *Phys. Rev. B* **93**, 054520 (2016).
 - [15] M. X. Wang, Y. Xu, L. P. He, J. Zhang, X. C. Hong, P. L. Cai, Z. B. Wang, J. K. Dong, and S. Y. Li, Nodeless superconducting gaps in noncentrosymmetric superconductor PbTaSe_2 with topological bulk nodal lines, *Phys. Rev. B* **93**, 020503(R) (2016).

- [16] G. M. Pang, M. Smidman, L. X. Zhao, Y. F. Wang, Z. F. Weng, L. Q. Che, Y. Chen, X. Lu, G. F. Chen, and H. Q. Yuan, Nodeless superconductivity in noncentrosymmetric PbTaSe₂ single crystals, *Phys. Rev. B* **93**, 060506(R) (2016).
- [17] U. Kaluarachchi *et al.*, Highly responsive ground state of PbTaSe₂: structural phase transition and evolution of superconductivity under pressure, *Phys. Rev. B* **95**, 224508 (2017).
- [18] R. Sankar *et al.* Anisotropic superconducting property studies of single crystal PbTaSe₂, *J. Phys.: Condens. Matter* **29**, 095601 (2017).
- [19] A. R. Oganov and C. W. Glass, Crystal structure prediction using ab initio evolutionary techniques: principles and applications, *J. Chem. Phys.* **124**, 244704 (2006).
- [20] A. R. Oganov, A. O. Lyakhov, and M. Valle, How evolutionary crystal structure prediction works and why, *Acc. Chem. Res.* **44**, 227 (2011).
- [21] A. O. Lyakhov, A. R. Oganov, H. T. Stokes, and Q. Zhu, New developments in evolutionary structure prediction algorithm USPEX, *Comput. Phys. Commun.* **184**, 1172 (2013).
- [22] P. Giannozzi *et al.* QUANTUM ESPRESSO: a modular and open-source software project for quantum simulations of materials, *J. Phys.: Condens. Matter* **21**, 395502 (2009).
- [23] J. P. Perdew, K. Burke M. Ernzerhof, Generalized Gradient Approximation Made Simple, *Phys. Rev. Lett.* **77**, 3865 (1996).
- [24] P. Blaha, K. Schwarz, G. K. H. Madsen, D. Kvasnicka and J. Luitz, WIEN2K, An Augmented Plane Wave + LO Program for Calculating Crystal Properties, TU Wien, Vienna (2001).
- [25] A. A. Mostofi, J. R. Yates, G. Pizzi, Y.-S. Lee, I. Souza, D. Vanderbilt, and N. Marzari, An updated version of WANNIER90: A tool for obtaining maximally-localised wannier functions, *Comput. Phys. Commun.* **185**, 2309 (2014).
- [26] Q. S. Wu, S. N. Zhang, H.-F. Song, M. Troyer, and A. A. Soluyanov, [arXiv:1703.07789](https://arxiv.org/abs/1703.07789).
- [27] Q. Li *et al.*, Chiral magnetic effect in ZrTe₅, *Nat. Phys.* **12**, 550 (2016).
- [28] S. K. Kushwaha *et al.*, Bulk crystal growth and electronic characterization of the 3D Dirac semimetal Na₃Bi, *APL Materials* **3**, 041504 (2015).
- [29] H. Chi, C. Zhang, G. D. Gu, D. E. Kharzeev, X. Dai and Q. Li, Lifshitz transition mediated electronic transport anomaly in bulk ZrTe₅, *New J. Phys.* **19**, 015005 (2017).
- [30] G. Bastien, A. Gourgout, D. Aoki, A. Pourret, I. Sheikin, G. Seyfarth, J. Flouquet, and G. Knebel, Lifshitz Transitions in the Ferromagnetic Superconductor UCoGe, *Phys. Rev. Lett.* **117**, 206401 (2016).
- [31] S. Baroni, S. de Gironcoli, A. Dal Corso, and P. Giannozzi, Phonons and related crystal properties from density-functional perturbation theory, *Rev. Mod. Phys.* **73**, 515 (2001).
- [32] W. Mcmillan, Transition temperature of strong-coupled superconductors, *Phys. Rev.* **167**, 331 (1968).
- [33] P. Allen and R. Dynes, Transition temperature of strong-coupled superconductors reanalyzed, *Phys. Rev. B* **12**, 905 (1975).